arXiv:1609.04760v1 [cond-mat.mtrl-sci] 15 Sep 2016

Structures and finite-temperature abundances of defects in In_2O_3-II from first-principles calculations

Jamie M. Wynn,[1,2] Richard J. Needs,[2] and Andrew J. Morris[2]

[1] *Centre for Scientific Computing, Cavendish Laboratory, University of Cambridge*
[2] *Theory of Condensed Matter Group, Cavendish Laboratory, University of Cambridge*

We have studied intrinsic defect complexes in In_2O_3 using *ab initio* random structure searching (AIRSS). Our first-principles density-functional-theory calculations predict the thermodynamic stability of several novel defect structures. We combine the static lattice energy and harmonic vibrational energy with the often-neglected configurational entropy to construct the free energy, which is minimised to predict defect abundances at finite temperatures. We predict that some of our new defect structures – in particular our $\{\mathrm{In},2V_\mathrm{O}\}$ and $\{2\mathrm{In},3V_\mathrm{O}\}$ defects – can exist in significant abundances at finite temperatures, and their densities of electronic states indicate that they could play an important role in the unexpectedly high density of n-type charge carriers observed in In_2O_3.

The thermodynamically most stable crystalline form of indium oxide (In_2O_3) is a transparent semiconducting oxide (TCO) that adopts the bixbyite structure. TCOs are relatively uncommon materials, but they are of significant technological interest. They combine the usually mutually exclusive properties of optical transparency in the visible range with high electrical conductivity. It has been observed that nominally undoped In_2O_3 exhibits intrinsic n-type conductivity, which has been associated with the presence of both oxygen vacancy defects [1, 2] and hydrogen impurities [3]. The aim of this work is to study the energetics and structures of low-energy defects in undoped In_2O_3.

Undoped In_2O_3 exhibits n-type conductivity with carrier concentrations of up to $10^{19}\,\mathrm{cm}^{-3}$ [4], even when grown in exceptionally pure environments [2]. This phenomenon is known as unintentional doping (UID). The UID in In_2O_3 was originally attributed to oxygen vacancies acting effectively as donors [4]; consistently with this, In_2O_3 is a non-stoichiometric material with an excess of In relative to O [4]. However, studies have been inconsistent on whether such vacancies are sufficiently shallow in energy to explain the effect [5, 6]. Other candidates which have been put forward to explain the unexpectedly high carrier density of In_2O_3 include indium self-interstitials [7] and hydrogen impurities [8]. Experimentally, the carrier density of In_2O_3 depends strongly on the temperature at which it is manufactured [3]. A great deal of research has been focused on optoelectronic applications of TCOs created by doping In_2O_3 with tin [9], which has been used in energy-efficient windows [10] and as an anode in OLEDs (organic light-emitting diodes) [11]. Undoped In_2O_3 also finds technological applications in gas sensors [12], and In_2O_3 nanotubes [13] have applications in arrays of nanotubes for biosensing [1].

Density-functional theory (DFT) has previously been used to elucidate the optical properties of In_2O_3 that give rise to its transparency [14] and to calculate formation energies of intrinsic point defects [9, 15]. In this work we go beyond previous studies by predicting the structures of defect complexes from first principles, which has allowed us to identify many new defects. We have used the *ab initio* random structure searching method (AIRSS) [16] to discover low energy defect structures. We have also incorporated finite-temperature effects in calculating their energetic stability. Previously AIRSS has been used to study phases of materials at high pressures [17], to determine structures of point defect complexes formed by impurities in silicon [18–20], to investigate zirconolite as a material for nuclear waste encapsulation [21, 22], and to map out the sequence of phase transitions in the lithiation and sodiation of phosphorus anodes in batteries [23].

Our calculations provide the static lattice energies, the configurational entropy accounting properly for the symmetries of defects, and the contribution of the phonons to the free energy. Each of these contributions can have a large impact on the defect abundances at ambient conditions. All DFT calculations reported in this letter were performed using the CASTEP plane-wave code [24]; the methodological details are provided in the Supplemental Material.

The bixbyite structure [25] of $Ia\bar{3}$ symmetry, also known as In_2O_3-II, is thermodynamically stable at ambient conditions. The structure contains two inequivalent types of In atom on the 8*b* and 24*d* Wyckoff sites. All oxygen atoms are equivalent and are on the 48*e* site.

In AIRSS a large number of random structures are generated using DFT methods and relaxed to the nearest local minimum of the energy landscape [16]. The structures that are particularly low in energy can then be singled out for further examination. The structure searching computations were performed using the 40-atom primitive cell of In_2O_3-II, and more accurate calculations on the most promising defects were performed in a 160-atom supercell.

The initial structures for the AIRSS searches were created by selecting a sphere of radius 3 Å centred on a random position within the In_2O_3 unit cell, and then removing atoms within the sphere at random and inserting In or O atoms. The atomic coordinates of all atoms within

the sphere were randomised, making sure that they were not unphysically close to one another.

We adopt throughout a notation in which defects are indicated by listing their contents within braces; we also use V_{x} to refer to a vacancy of element x so that, for example, {In, V_{O}} constitutes an indium substitutional. Metastable defects are indicated using asterisks; for example, the lowest-energy oxygen vacancy would be denoted using $\{V_{\mathrm{O}}\}$, the second-lowest as $\{V_{\mathrm{O}}\}^*$, and the third-lowest as $\{V_{\mathrm{O}}\}^{**}$.

Because In_2O_3 empirically exhibits a deficit of oxygen relative to its ideal bulk stoichiometry, we searched for defects formed by a mixture of oxygen vacancies and indium interstitials. These searches generated a total of 632 defect structures (although many of them are duplicates). To our knowledge, none of the 'nontrivial' defects found here – *i.e.*, anything but single-atom interstitials, vacancies, and substitutionals – has been reported previously in the literature.

Defect abundances at finite temperatures are calculated by constructing the free energy and minimising it with respect to the abundances. Our expression for the free energy takes into account contributions from the static-lattice formation energies, phonons, and the configurational entropy associated with the defects:

$$F = \sum_i n_i E_i + \sum_i n_i F_i^{\mathrm{vib}} - k_B T \ln\left(\frac{N!\prod_i w_i^{n_i}}{(N-\sum_i n_i)!\prod_i n_i!}\right), \quad (1)$$

where the n_i are the number of defects of type i, N is the total number of lattice sites, w_i is the configurational degeneracy per lattice site, F_i^{vib} is the temperature-dependent vibrational free energy, and E_i is the formation energy of the i-th defect.

The vibrational free energy is given within the harmonic approximation by [26] $F_i^{\mathrm{vib}} = k_B \int g_i(\omega) \ln(2\sinh(\beta\hbar\omega))\mathrm{d}\omega$, where $g_i(\omega)$ is the phonon density of states of the i-th defect. We calculate the configurational degeneracies w_i of the defects by applying each symmetry operator of the space group of bulk In_2O_3 and counting the number of differently oriented versions of the same defect that are thereby generated. (In the calculation of the w_i, we count defects which differ only by a translation as the same, since the entropy associated with placing a defect on different lattice sites is already included in Eq. 1.) The logarithm of the degeneracy then gives the orientational configurational entropy per lattice site (divided by k_B), as described in Ref. 27. Along with a contribution from the combinatorics of assigning the defects to particular lattice sites, this forms the third term of Eq. 1. The defect abundances are computed by minimising Eq. 1 with respect to the n_i at some particular temperature, T.

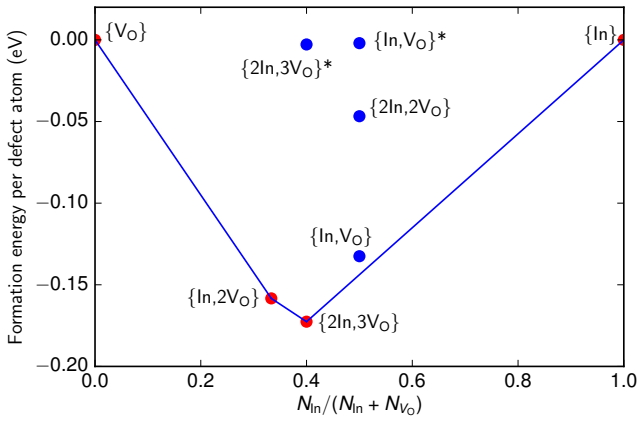

FIG. 1. Convex hull for defect complexes in In_2O_3 consisting of oxygen vacancies and indium interstitials. The convex hull is shown in blue. Defects lying on the hull are red, and those above the hull are blue.

The formation energy of a defect is defined as [28]

$$E_F = E_D - \sum_\alpha N_\alpha \mu_\alpha - E_B. \quad (2)$$

In the above, N_α is the number of defect atoms of species α; the μ_α are the associated chemical potentials; E_D is the total energy of the defective unit cell; and E_B is the total energy of the bulk unit cell.

To visualise the energetics of the binary defects generated by the structure searching, we use the Maxwell construction, which has previously been applied to defects in Ref. 18. The Maxwell construction is obtained by plotting the formation energy per atom of each defect against its composition. At $T = 0$, only those defects lying on the convex hull of the resulting scatter plot are thermodynamically stable.

The Maxwell construction for the most energetically favorable defects after re-optimisation in the larger 160-atom unit cell is shown in Fig. 1. Note that we treat vacancies just as we would atoms, so that in Fig. 1, the x-axis runs from the case where there are oxygen vacancies but no indium interstitials to the case where there are indium interstitials but no oxygen vacancies. Fig. 1 shows how the two types of defect bind as a function of their concentrations relative to each other. The chemical potentials for V_{O} and In were calculated using the oxygen vacancy and indium interstitial defects, with $\mu_{V_{\mathrm{O}}} = E(\{V_{\mathrm{O}}\}) - E_B$. (We note that the convex hull ceases to be meaningful at $T > 0$, since Eq. 1 shows that the entropy is a nonlinear function of the defect concentrations.)

We now survey the structures of the defects whose energies are reported in Fig. 1. The lowest-energy indium interstitial was found to be the c-site defect previously reported in Ref. 9. Since all oxygen atoms in In_2O_3 occupy the same Wyckoff site, there is only one way to remove

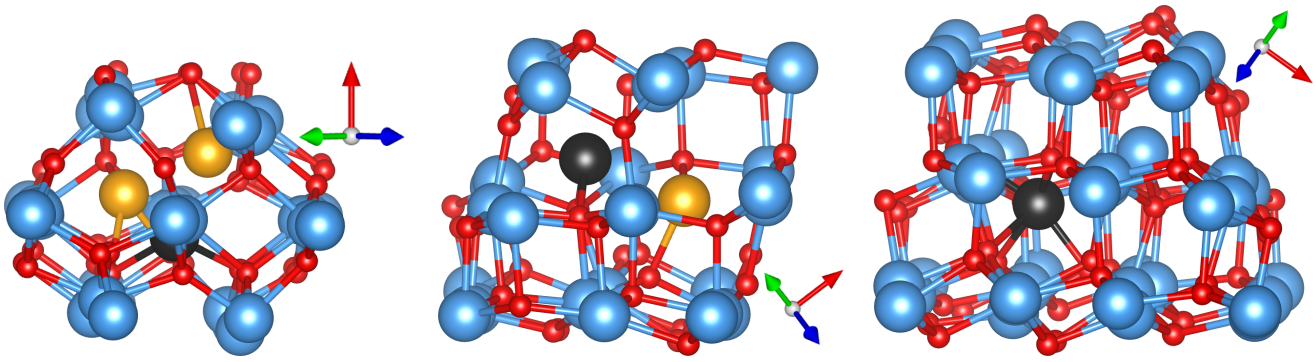

(a) (b) (c)

FIG. 2. Left to right, the $\{2\mathrm{In},3V_\mathrm{O}\}$, $\{\mathrm{In},2V_\mathrm{O}\}$ and $\{\mathrm{In},V_\mathrm{O}\}$ defects. For visual clarity we show only the structure in the vicinity of the defect, rather than the entire unit cell. Indium atoms are shown in blue and oxygen atoms in red. (Black and orange indium atoms are referred to specifically in the text.) Lattice vectors of the conventional cubic unit cell are shown next to each defect, although they are not labelled because under the $Ia\bar{3}$ space group the three lattice vectors are symmetrically equivalent.

an oxygen atom, leading to a single possible O vacancy defect (barring significant disruption to the lattice in its vicinity, which we find to be energetically unfavorable).

The defect with the lowest formation energy was found to be $\{2\mathrm{In},3V_\mathrm{O}\}$, which is shown in Fig. 2(a). In this defect, two In atoms (orange) sit either side of an In site as in a split interstitial. This is accommodated by the removal of 3 O atoms and the significant displacement of another In atom (black) away from the defect. The $\{\mathrm{In},2V_\mathrm{O}\}$ defect shown in Fig. 2(b) is also on the convex hull and consists of an interstitial indium atom (black) with partially ionic bonds to two nearby oxygen atoms, which significantly displace a nearby indium atom (orange, to its lower-right). The $\{\mathrm{In},V_\mathrm{O}\}$ defect, consisting of an In substitutional as shown in Fig. 2(c), is close enough to the hull to become potentially relevant at finite temperatures, given the intrinsic errors in DFT calculations. In this defect, an In atom (black) substitutes for an O atom, which significantly displaces the closest In atom, which is visible to its top-right in Fig. 2(c). To our knowledge, these defect structures have not been reported previously in the literature except for the indium interstitial and oxygen vacancy at the endpoints of the convex hull from which the chemical potentials were taken. The metastable $\{2\mathrm{In},2V_\mathrm{O}\}$, $\{\mathrm{In},V_\mathrm{O}\}$*, and $\{2\mathrm{In},3V_\mathrm{O}\}$* defects shown in Fig. 1 are described in the Supplemental Material.

Having identified the structures of defect complexes formed from oxygen vacancies and indium interstitials, their capacity to act as shallow donors was studied by calculating their densities of electronic states (DOS); if any of the defects identified create occupied states close to the conduction band, they are potentially implicated in the intrinsic n-type doping that is observed in In_2O_3. We investigated the DOS of each defect lying close to the convex hull, and obtained the results shown in Fig. 3, given alongside the bulk DOS for reference. This was done for each defect lying close to the convex hull. The densities of states were calculated using CASTEP and the adaptive broadening functionality [29] of the OptaDOS [30] code.

As is typical, the PBE functional significantly underestimates the band gap of In_2O_3; our calculations produce a gap of 0.8 eV, compared to an experimental value of around 3 eV. It is therefore possible, in principle, that the presence of occupied defect levels near the bottom of the valence band is simply the result of the inaccurately small gap predicted by the PBE functional. We tested this by recalculating the DOS for the oxygen vacancy using the HSE06 [31] screened exchange functional which gives larger and more accurate band gaps than PBE. By comparing the densities of states with the PBE and HSE06 functionals, we find that using an accurate band gap shifts the defect levels shift upwards with the conduction band rather than being fixed with respect to the valence band. This dispels concerns that the shallowness of the defect levels relative to the valence band may be an artifact of the unphysically small PBE band gap. (The two densities of states are shown in the Supplemental Material.)

After predicting the defects and their structures, we next predicted their abundances at finite temperatures using the methods described previously. Harmonic phonon calculations were performed for all of the 160-atom defect cells and the free energy was constructed and minimised using Eq. 1. Such calculations were repeated for a range of temperatures and stoichiometries, giving the defect abundances as a function of temperature and stoichiometry. This allows the construction of the phase diagram shown in Fig. 4 in which the x-axis gives the relative concentration of oxygen vacancies and indium interstitials as in Fig. 1.

The phase diagram indicates that finite temperature

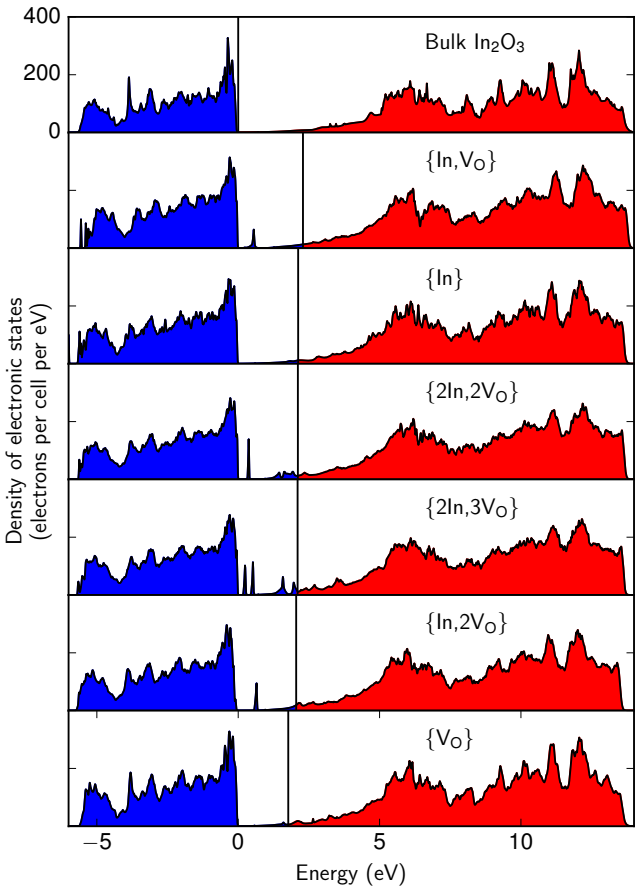

FIG. 3. Electronic density of states (DOS) of the low-lying In_2O_3 defects shown in Fig. 1, together with the bulk density of states for comparison. Above the VBM, each DOS has been multiplied by a factor of 2 for visual clarity. The Fermi level is shown in each case by a vertical black line. All DOS have been shifted in order to align their VBMs. Occupied states are shown in blue and unoccupied states are shown in red. Tick marks on each DOS match those shown at the top.

effects are highly significant, with the $\{2\text{In},3\,V_\text{O}\}$ defect dissociating almost entirely above room temperature. This is because the configurational entropy is maximised by breaking composite defects into multiple smaller defects. This entropically driven dissociation leads, once the $\{2\text{In},3\,V_\text{O}\}$ defects have largely dissociated, to the formation of a higher number of $\{\text{In},2\,V_\text{O}\}$ defects over certain temperature ranges, until the temperature increases still further and entropy maximisation dominates over energy minimisation so that the defect complexes break up completely and the $\{V_\text{O}\}$ and {In} point defects no longer bind to each other. (We have also recomputed the phase diagram using only those defects which had appeared in the literature prior to this paper, and the results confirm that our new defects significantly alter the predicted interaction between oxygen vacancies and indium interstitials; the recomputed phase diagram is shown in the Supplemental Material.)

We find the impact of the orientational degeneracy term to be very significant: by recomputing the phase diagram with translational entropy included but orientational entropy ignored, we calculate that the inclusion of the orientational degeneracy term pushes the temperature above which the $\{\text{In},2\,V_\text{O}\}$ defect constitutes under 10% of all defects from 820 K down to the 500 K shown in Fig. 4. This can be understood once again as an entropically driven destabilisation of larger defect complexes such as $\{\text{In},2\,V_\text{O}\}$ relative to their dissociation into smaller defects. We note that the magnitude of this change – a full 320 K shift in the transition temperature at which $\{\text{In},2\,V_\text{O}\}$ dissociates – demonstrates the importance of capturing the effects of orientational entropy, as we have done here using our group theory scheme. (The recalculated phase diagram without orientational entropy included is also shown in the Supplemental Material.)

The defect structures, formation energies, degeneracies, and sources (AIRSS or literature) are summarised in Table I. Note that the large number of defects with a degeneracy of 24 arises because the primitive cell of In_2O_3 has 24 symmetry operators, and most of the defects break all of the symmetries of the bulk.

In conclusion, we have implemented a general methodology for first-principles predictions of defect abundances in crystalline materials at finite temperature. This methodology has been applied to bixbyite In_2O_3. Vibrational corrections and defect degeneracies are included in the free energies, which has led to the prediction of novel defect complexes from first principles. Using a group theory method, we have calculated the important but often-neglected contribution of the orientational degeneracy to the defect free energies, which has allowed us to provide a more accurate prediction of the abundances of the defects than has been possible to obtain before.

Studies of the intrinsic doping of In_2O_3 have focused on the oxygen vacancy and indium interstitial defects as possible causes, but the results of our structure searches suggest that these point defects in fact tend to bind to each other to form composite defects whose structures we have described here for the first time; moreover, our finite-temperature calculations suggest that they remain bound at ambient conditions. By calculating the electronic DOS of these defects, we have also shown that they have the potential to act as shallow donors, which provide a source of charge carriers. These results could have significant implications for the question of the cause of intrinsic doping in In_2O_3, whose origin has been the subject of ongoing controversy. Given experimental findings that the conductivity of In_2O_3 varies significantly with its annealing temperature, our calculations could also offer greater insight into the underlying defect physics affecting the manufacturing process.

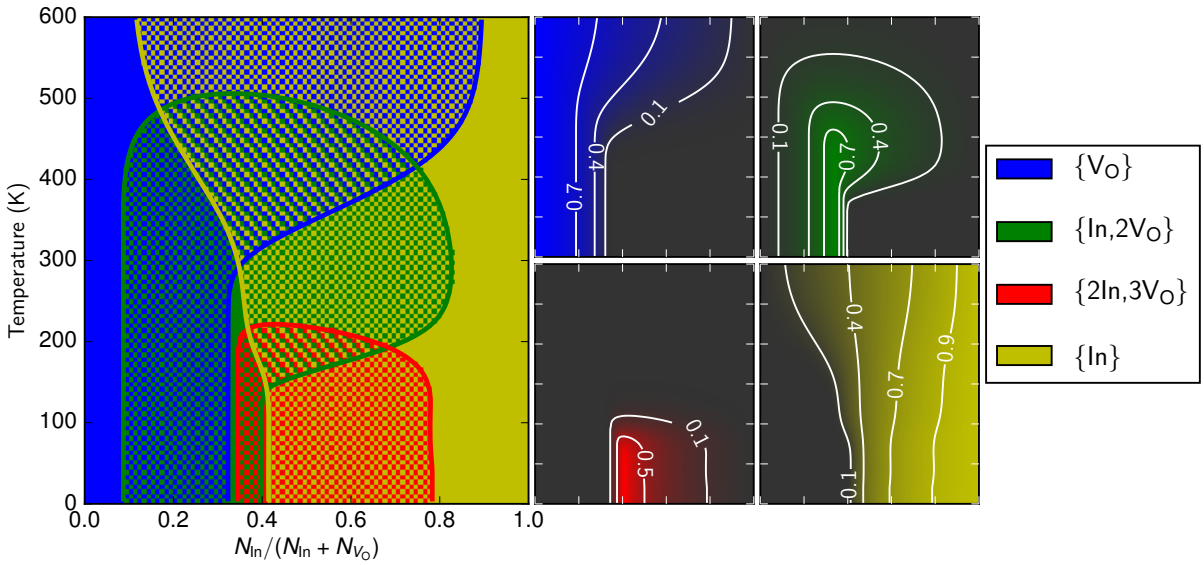

FIG. 4. Relative abundances of defect complexes of O vacancies and In interstitials in In_2O_3. Contours are plotted on the main panel where each defect constitutes 10% of all defects present; likewise, the 'checkerboard' pattern indicates which defects form at least 10% of all defects present. On each of the smaller panels on the right, the relative abundance of each defect is plotted to show more precisely how it varies, along with contour lines of equal relative abundance. In these smaller subplots, the colouring, axis ranges and tick marks correspond with those on the main panel.

Defect	E_F/atom	Degeneracy	Origin
{In,2V_O}	-0.16	24	AIRSS
{In,V_O}	-0.13	24	Known [9]
{In,V_O}*	0.00	24	AIRSS
{2In,2V_O}	-0.05	24	AIRSS
{In}	0.00	4	Known [32]
{2In,3V_O}*	0.00	24	AIRSS
{V_O}	0.00	24	Known [33]
{2In,3V_O}	-0.17	24	AIRSS

TABLE I. Each defect appearing in this study is reported, along with its $T = 0$ formation energy per atom, orientational degeneracy, and origin. All of the structures in this Table were found by AIRSS, but those marked as 'AIRSS' are believed to have been found in this study for the first time, whereas those whose origin is 'Known' have appeared previously in the literature. The formation energies of {V_O} and {In} are zero by definition, since we have used them as the reservoirs of oxygen vacancies and indium interstitials.

R. J. N. acknowledges financial support from the Engineering and Physical Sciences Research Council (EPSRC) of the U.K. [EP/J017639/1]. This work was performed using the Darwin Supercomputer of the University of Cambridge High Performance Computing Service (http://www.hpc.cam.ac.uk/), provided by Dell Inc. using Strategic Research Infrastructure Funding from the Higher Education Funding Council for England and funding from the Science and Technology Facilities Council. R. J. N. and A. J. M. acknowledge use of the Archer facilities of the U.K.'s national high-performance computing service (for which access was obtained via the UKCP consortium EP/K014560/1). J. M. W. acknowledges the support of the EPSRC Centre for Doctoral Training in Computational Methods for Materials Science. A. J. M. acknowledges support from the Winton Programme for the Physics of Sustainability.

Data used in this work are available via the Cambridge data repository at dx.doi.org/10.17863/CAM.4396.

We are grateful to Chris G. Van De Walle for fruitful discussions.

[1] M. Curreli, C. Li, Y. Sun, B. Lei, M. A. Gundersen, M. E. Thompson, and C. Zhou, Journal of the American Chemical Society **127**, 6922 (2005).
[2] O. Bierwagen, Semiconductor Science and Technology **30**, 24001 (2015).
[3] Z. Galazka, K. Irmscher, M. Pietsch, T. Schulz, R. Uecker, D. Klimm, and R. Fornari, Cryst. Eng. Comm. **15**, 2220 (2013).
[4] J. H. W. De Wit, G. Van Unen, and M. Lahey, Journal of Physics and Chemistry of Solids **38**, 819 (1977).
[5] S. Limpijumnong, P. Reunchan, A. Janotti, and C. G. Van De Walle, Physical Review B - Condensed Matter and Materials Physics **80**, 193202 (2009).
[6] O. Bierwagen and J. S. Speck, Appl. Phys. Lett. **101**, 102107 (2012).
[7] L.-M. Tang, L.-L. Wang, D. Wang, J.-Z. Liu, and K.-Q. Chen, Journal of Applied Physics **107**, 83704 (2010).
[8] P. D. C. King, R. L. Lichti, Y. G. Celebi, J. M. Gil, R. C. Vilao, H. V. Alberto, J. Piroto Duarte, D. J. Payne, R. G.

Egdell, I. McKenzie, C. F. McConville, S. F. J. Cox, and T. D. Veal, Physical Review B - Condensed Matter and Materials Physics **80**, 081201 (2009).
[9] P. Agoston, P. Erhart, A. Klein, and K. Albe, Journal of Physics: Condensed Matter **21**, 455801 (2009).
[10] I. Hamberg and C. G. Granqvist, Journal of Applied Physics **60**, R123 (1986).
[11] N. G. Park, M. Y. Kwak, B. O. Kim, O. K. Kwon, Y. K. Kim, B. You, T. W. Kim, and Y. S. Kim, Jpn. J. Appl. Phys. **41**, 1523 (2002).
[12] X. Xu, D. Wang, J. Liu, P. Sun, Y. Guan, H. Zhang, Y. Sun, F. Liu, X. Liang, Y. Gao, and E. al., Sensors and Actuators B: Chemical **185**, 32 (2013).
[13] X.-P. Shen, H.-J. Liu, X. Fan, Y. Jiang, J.-M. Hong, and Z. Xu, Journal of Crystal Growth **276**, 471 (2005).
[14] A. Walsh, J. L. F. Da Silva, S.-H. Wei, C. Körber, A. Klein, L. F. J. Piper, A. DeMasi, K. E. Smith, G. Panaccione, and P. Torelli, Physical Review Letters **100**, 167402 (2008).
[15] P. Ágoston, K. Albe, R. M. Nieminen, and M. J. Puska, Phys. Rev. Lett. **103**, 245501 (2009).
[16] C. J. Pickard and R. J. Needs, J. Phys.: Condens. Matter **23**, 53201 (2011).
[17] C. J. Pickard and R. J. Needs, Physical Review Letters **97**, 045504 (2006).
[18] A. J. Morris, C. P. Grey, R. J. Needs, and C. J. Pickard, Phys. Rev. B **84**, 224106 (2011).
[19] A. J. Morris, C. J. Pickard, and R. J. Needs, Phys. Rev. B **80**, 144112 (2009).
[20] A. J. Morris, R. J. Needs, E. Salager, C. P. Grey, and C. J. Pickard, Phys. Rev. B **87**, 174108 (2013).
[21] J. Mulroue, A. J. Morris, and D. M. Duffy, Phys. Rev. B **84**, 094118 (2011).
[22] J. Mulroue, M. Watkins, A. J. Morris, and D. M. Duffy, Journal of Nuclear Materials **437**, 261 (2013).
[23] M. Mayo, K. J. Griffith, C. J. Pickard, and A. J. Morris, Chemistry of Materials **28**, 2011 (2016), arXiv:1510.03248.
[24] S. J. Clark, M. D. Segall, C. J. Pickard, P. J. Hasnip, M. I. J. Probert, K. Refson, and M. C. Payne, Zeitschrift fur Kristallographie **220**, 567 (2005).
[25] S. Z. Karazhanov, P. Ravindran, P. Vajeeston, A. Ulyashin, T. G. Finstad, and H. Fjellvåg, Phys. Rev. B **76**, 075129 (2007).
[26] O. K. Al-Mushadani and R. J. Needs, Phys. Rev. B **68**, 235205 (2003).
[27] A. J. Morris, C. J. Pickard, and R. J. Needs, Physical Review B **78**, 184102 (2008).
[28] C. Freysoldt, B. Grabowski, T. Hickel, J. Neugebauer, G. Kresse, A. Janotti, and C. G. Van De Walle, Reviews of Modern Physics **86**, 253 (2014).
[29] J. R. Yates, X. Wang, D. Vanderbilt, and I. Souza, Physical Review B **75**, 195121 (2007).
[30] A. J. Morris, R. J. Nicholls, C. J. Pickard, and J. R. Yates, Computer Physics Communications **185**, 1477 (2014).
[31] A. V. Krukau, O. A. Vydrov, A. F. Izmaylov, and G. E. Scuseria, The Journal of Chemical Physics **125**, 224106 (2006).
[32] T. Tomita, K. Yamashita, Y. Hayafuji, and H. Adachi, Applied Physics Letters **87**, 051911 (2005).
[33] I. Tanaka, M. Mizuno, and H. Adachi, Physical Review B **56**, 3536 (1997).

arXiv:1609.04760v1 [cond-mat.mtrl-sci] 15 Sep 2016

Structures and finite-temperature abundances of defects in In_2O_3-II from first-principles calculations: supplementary information

Jamie M. Wynn, Richard J. Needs, and Andrew J. Morris

Theory of Condensed Matter Group, Cavendish Laboratory, University of Cambridge

Structure searching

All density-functional theory (DFT) calculations were performed using version 8 of the CASTEP [1] plane-wave code. In the initial structure search we used Vanderbilt ultrasoft pseudopotentials [2] generated by CASTEP. In these pseudopotentials the $4d$, $5s$ and $5p$ electrons in indium were treated as valence electrons and the others as core electrons, while for oxygen the $2s$ and $2p$ electrons were treated as valence electrons[1].

By performing a series of total energy calculations, we found that a cutoff of 500 eV is sufficient to obtain formation energies to within 12 meV which is accurate enough for the purposes of the initial AIRSS searches. We performed the searches in the 40-atom primitive unit cell shown in Fig. 1. The Brillouin zone (BZ) was sampled using only the Baldereschi mean-value point [3], which we find is associated with a sampling error of less than 0.02 eV per atom. We used the lattice constant obtained from the PBE functional of 10.21 Å which is in agreement with the PBE results presented in Ref. 4 and is 0.8% larger than the experimental value [5].

Supercell calculations

After the initial structure searching phase, the structures of the defects lying closest to the convex hull were refined by re-optimising them in a larger cell with more accurate computational settings. We used a 160-atom supercell

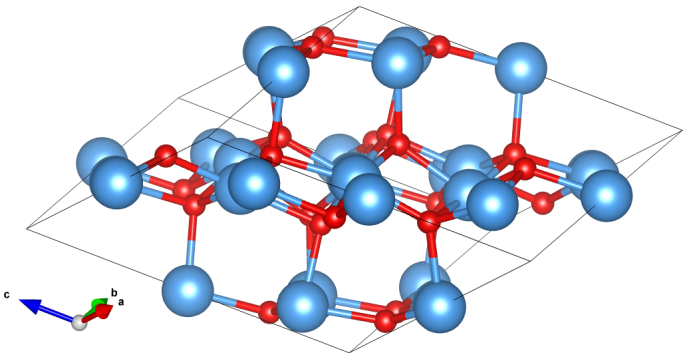

FIG. 1. The 40-atom primitive unit cell of In_2O_3 used for structure searching in this work. Oxygen atoms are in red, and indium atoms are blue. The structure is shown along the [112] direction, which reveals it to be slightly displaced from a series of planes of O and In atoms.

[1] The CASTEP pseudopotential generation strings used to generate the pseudopotentials were `3|2.3|6|8|8|50:51:42` for indium, and `2|1.1|14|16|19|20:21(qc=7)` for oxygen.

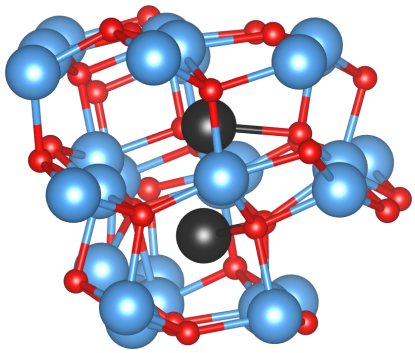

FIG. 2. The {2In,2V_O} defect: two In interstitials lie either side of a layer of In atoms, with each of them forming ionic bonds with two nearby O atoms.

with the shape chosen to maximise the distance from each defect to its nearest periodic image. This supercell is the primitive cell of a face-centred cubic lattice, with lattice parameters $a = b = c = 14.44$ Å and angles $\alpha = 60°$, $\beta = 60°$ and $\gamma = 90°$.

The geometry optimisation in the 160-atom supercell was performed with a higher basis set cutoff of 700 eV and BZ sampling on a $2 \times 2 \times 2$ Monkhorst-Pack grid. We use the same ultrasoft pseudopotentials as for the initial search.

We calculate (via calculations performed at still higher basis cutoffs) that truncating the plane wave basis beyond 700 eV results in an error in the formation energies of under 2 meV per atom. Some calculations performed with a $4 \times 4 \times 4$ MP grid indicate that the corresponding error in the total energy due to the BZ sampling is under 4 meV per atom.

To calculate the vibrational free energy of a defect, we first relax the 160-atom supercell containing that defect so that the forces on the atoms are no larger than 0.01 eV Å^{-1}. We then perform harmonic phonon calculations using the finite-difference method, solving the Kohn-Sham equations at Γ only (due to the significant cost of phonon calculations on such large cells and the fact that the phonon free energy is generally a small correction). The elements of the dynamical matrix were evaluated using the finite displacement method, and only phonons with wavevector $\mathbf{q} = 0$ were considered.

Metastable defects

Because their relative energetic unfavourability renders them of lesser physical importance, three metastable defect structures were not shown in the Letter. Nevertheless, they are novel structures and are predicted to be stable relative to dissociation into isolated indium interstitials and oxygen vacancies, so we show them here. In the {2In,2V_O} (pictured in Fig. 2), two In interstitials (black) sit above and below a layer of In atoms, and each binds to two nearby O atoms (similarly to {In,2V_O}). The {In,V_O}* defect is a split indium interstitial shown on Fig. 3, whilst the larger {2In,3V_O}* complex consists of two split In interstitials in close proximity, and is shown on Fig. 4.

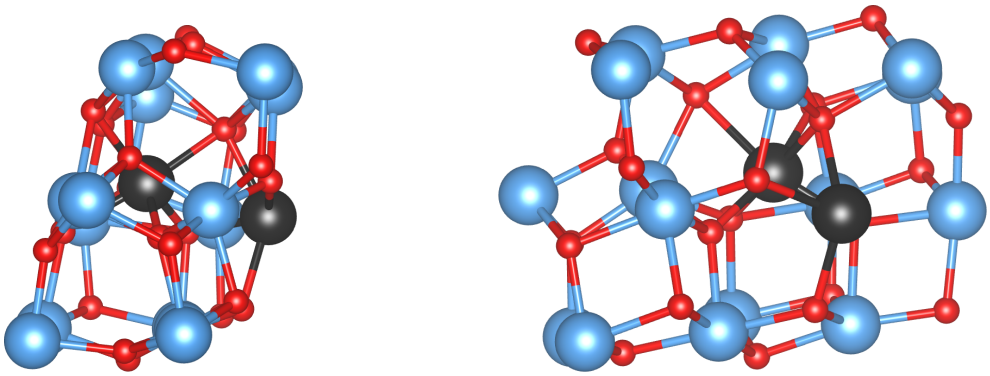

(a) (b)

FIG. 3. The $\{\mathrm{In}, V_\mathrm{O}\}$* defect: an In split interstitial (dark black), combined with significant repositioning of nearby oxygen atoms.

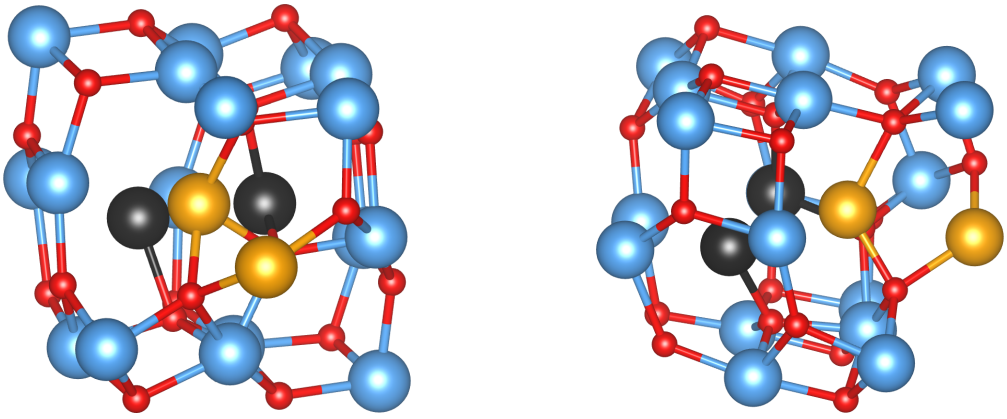

(a) (b)

FIG. 4. The $\{2\mathrm{In},3\,V_\mathrm{O}\}$* defect: two In split interstitials (one in black, one in orange) are positioned so that the orange interstitial points into the site about which the first interstitial forms.

Finite-temperature abundances

To illustrate the effects of both the novel defects we have discovered, and of our inclusion of the configurational entropy term, we have recalculated the phase diagram without each of these factors. The resulting phase diagrams (Fig. 5) show markedly different behaviour: the simple $\{\mathrm{In}, V_\mathrm{O}\}$ indium substitutional is not as energetically favourable as the new $\{2\mathrm{In},3\,V_\mathrm{O}\}$ and $\{\mathrm{In},2\,V_\mathrm{O}\}$ defects, and as a result it has largely dissociated at room temperature. The significance of the configurational entropy term is also clear on Fig. 5, with a marked decrease in the stability of the composite $\{2\mathrm{In},3\,V_\mathrm{O}\}$ and $\{\mathrm{In},2\,V_\mathrm{O}\}$ defects when the effects of configurational entropy are taken into account.

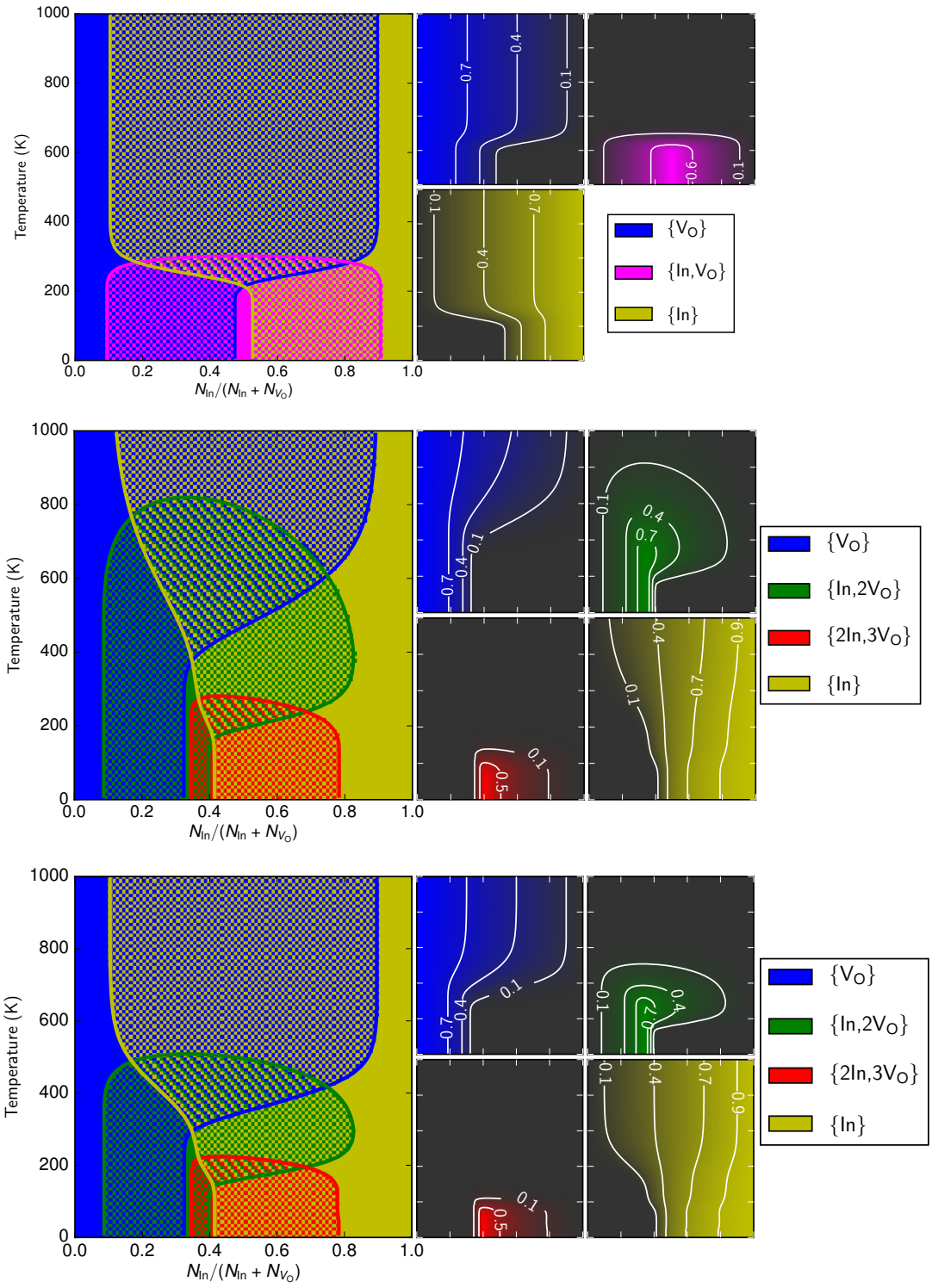

FIG. 5. The defect phase diagram calculated using only previously known defects (top), including newly found defects but ignoring the effect of orientational entropy (middle), and – for comparison – including both new defects and orientational entropy (bottom), as in Fig. 4 of the main text. As with the phase diagram in the main text, the smaller subpanels show the relative abundance of each defect along with contours of equal relative abundance.

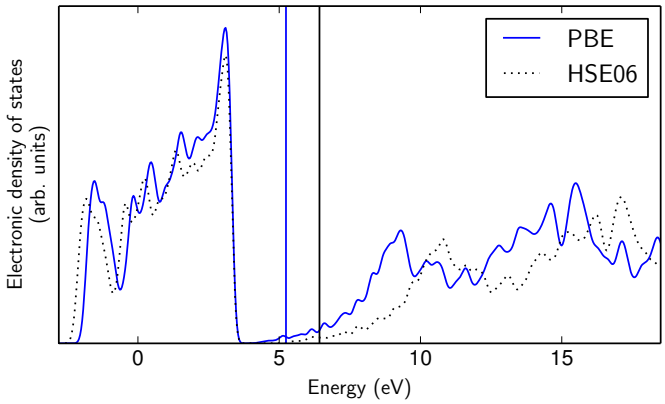

FIG. 6. Electronic density of states in the vicinity of the band gap for the $\{V_O\}$ defect, computed with the PBE and HSE06 functionals. The densities of states have been shifted to align their VBMs, and the Fermi levels for the two functionals are indicated by vertical lines.

HSE06 calculations

In our HSE06 density of states calculations we use the conventional cubic 80-atom unit cell with the Kohn-Sham equations solved self-consistently at the Γ point of the BZ only (because of the extreme cost of computing the screened exchange term), before solving the Kohn-Sham equations non-self-consistently on a $5 \times 5 \times 5$ Monkhorst-Pack grid. (We choose an odd n for the MP grid because In_2O_3-II has a direct band gap at Γ; this would be a suboptimal choice for the calculation of total energies, but for densities of states it gives more accurate energies for the valence band maximum and conduction band minimum.) Norm-conserving pseudopotentials were used which treated as valence the indium $4d$, $5s$ and $5p$ orbitals and the oxygen $2s$ and $2p$ orbitals. We increased the plane wave basis set cutoff to 850 eV for these calculations. The resulting density of states is shown alongside that resulting from the PBE functional is shown on Fig. 6; both densities of states are calculated using version 1.2 of the OptaDOS [6, 7] code.

[1] S. J. Clark, M. D. Segall, C. J. Pickard, P. J. Hasnip, M. I. J. Probert, K. Refson, and M. C. Payne, Zeitschrift fur Kristallographie **220**, 567 (2005).

[2] D. Vanderbilt, Physical Review B **41**, 7892 (1990).

[3] A. Baldereschi, Physical Review B **7**, 5212 (1973).

[4] J. B. Varley and A. Schleife, Semicond. Sci. Technol. **30**, 24010 (2015).

[5] M. Marezio, Acta Cryst **20**, 723 (1966).

[6] J. R. Yates, X. Wang, D. Vanderbilt, and I. Souza, Physical Review B **75**, 195121 (2007).

[7] A. J. Morris, R. J. Nicholls, C. J. Pickard, and J. R. Yates, Computer Physics Communications **185**, 1477 (2014).